PAPER • OPEN ACCESS

Modelling of the effect of particle species on beam losses in W7-X

To cite this article: L. Sanchis *et al* 2026 *Nucl. Fusion* **66** 026046

OPEN ACCESS
IOP Publishing | International Atomic Energy Agency
Nuclear Fusion
Nucl. Fusion **66** (2026) 026046 (18pp)
https://doi.org/10.1088/1741-4326/ae2f6f

Modelling of the effect of particle species on beam losses in W7-X

L. Sanchis[1,*], T. Kurki-Suonio[2], K. Särkimäki[3], P. Ollus[2,a], J. Kontula[2], S. Äkäslompolo[2], S. Lazerson[4], S. Bozhenkov[5], H.M. Smith[5] and the W7-X Team[b]

[1] Department of Atomic, nuclear and molecular physics, University of Sevilla, Sevilla, Spain
[2] Department of Applied Physics, Aalto University, FI-00076 Aalto, Finland
[3] VTT Technical Research Centre of Finland Ltd, Espoo, Finland
[4] Gauss Fusion GmbH, Garching bei München, Germany
[5] Max-Planck-Institut für Plasmaphysik, Greifswald, Germany

E-mail: lsanchis@us.es

Received 18 September 2025, revised 14 December 2025
Accepted for publication 19 December 2025
Published 21 January 2026

Abstract

In Wendelstein 7-X (W7-X), future campaigns will include H, D and He as both NBI injection and target plasmas but, so far, only H injection and target plasmas have been extensively performed. The species effect on the beam-ion confinement and associated power loads has been studied with the ASCOT code to estimate the location and intensity of the hot spots. For this analysis, standard, high and low mirror configurations were considered to provide results covering the variation of the mirror term most likely to affect the beam-ion behaviour. Beam-ion losses were highest for D beams and lowest for He beams. Changing the target plasma from hydrogenic species to helium also produced higher losses. Hot-spot analysis showed peak loads up to 3 MW m^{-2} for D beams, with 1 MW m^{-2} and 0.1 MW m^{-2} for H and He beams, respectively. Losses were predominantly to carbon components independent of the mirror term. This is particularly apparent for the low-mirror configuration, showing that 97%–99% of the power loads avoid the more delicate steel components. The results of the helium injection and target plasmas can be validated against experimental results in the upcoming campaign to support the results for the deuterium modelling.

Keywords: fast ions, Monte Carlo, ASCOT, stellarator, W7-X, NBI, helium

(Some figures may appear in colour only in the online journal)

[a] Current affiliation: Department of Physics and Astronomy, Uppsala University, Uppsala SE-751 20, Sweden.
[b] See Grulke *et al* 2024 (https://doi.org/10.1088/1741-4326/ad2f4d) for the W7-X Team.
[*] Author to whom any correspondence should be addressed.

1. Introduction

The Wendelstein 7-X (W7-X) stellarator is equipped with two neutral beam injector heating systems designed to operate with hydrogen, deuterium and helium injections at 55 keV, 60 keV and 40 keV respectively [1, 2]. Ideally, all the injected neutrals would be ionised in the plasma, preferably deep in the core, depositing their energy to the target plasma thus elevating its temperature. Unfortunately, both particle deposition and confinement depend on plasma parameters, leading to associated power losses. In the case of shinethrough, the injected neutral fails to ionise and strikes the wall components after traversing the plasma ballistically. Even neutrals that do get ionised can be lost due to net radial displacements and neoclassical transport caused by drifts and collisions [3]; these losses correspond to beam-ion losses. Considering the wall integrity, high power loads due to ion losses are most critical. Obviously, the shinethrough particles hit the beam-dump wall structures at their injection energy and, thus, this loss mechanism should be minimised. In axisymmetric tokamaks, prompt losses can occur for beam ions born on unconfined orbits at injection energy, mostly at near-perpendicular injections. However, losses generally arise only after substantial slowing down, predominantly through transport mechanisms such as energetic-particle modes [4–7], magnetohydrodynamic modes [8, 9], resonant interactions [10–12] and edge banana orbits. However, in a non-axisymmetric stellarator, in addition to losses due to particles being born on unconfined orbits, beam ions can be lost due to collisionless changes in the orbit topologies [3].

Beam-ion simulations using the Monte-Carlo orbit-following code ASCOT [13] were performed in preparation for the previous campaigns to predict power loads on vulnerable plasma-facing components (PFCs) caused hydrogen injection [14, 15]. Helium injection, first implemented during the plasma scientific operation OP2.2, was maintained throughout OP2.3 and is planned to continue through OP2.4 and OP2.5 campaigns. During OP2.2 and OP2.3, the effect of the species charge-to-mass ratio was studied in a number of experiments using helium and hydrogen target plasmas, some of which employed the NBI system. The interpretation of the experimental data requires dedicated modelling of the hydrogen and helium beams in both hydrogen and helium plasmas to investigate the underlying ion transport. In preparation for OP2.4 and OP2.5, modelling will assess beam-ion losses in the standard (STD), high-mirror (HM), and low-mirror (LM) configurations and optimise operating parameters to maintain power loads within safety limits. Although not planned for near-term operation, D-beam injections were also included in this analysis as they offer valuable input for predictive modelling and scenario development.

Previous studies on DIII-D have indicated that the fast-ion distribution depends on both the species of the injected particles and the species of the background plasma. The way different MHD modes and ion-cyclotron-range instabilities are driven also has species dependencies [16, 17]. While these effects were broadly consistent with theoretical and modelling expectations, the detailed patterns often deviated from predictions, reflecting the complex interplay of species in experiments. Related experiments on AUG and MAST-U have also examined species-dependent fast-ion behaviour [18, 19]. The present model provides a framework for future studies that include MHD effects and can help interpret such multispecies experimental observations.

This study analyses hydrogen, deuterium and helium beam injections into various plasma species including hydrogen, deuterium and helium plasma. The STD, HM and LM magnetic configurations have been simulated to identify the wall components that are potentially at risk of exceeding the safety limits of heat loads as well as to analyse the beam-ion loss channels. The assessment of vulnerable components is mainly focused on the steel components of the wall, including panels, ports and vacuum vessel.

The prediction capabilities of the beam-ion modelling have been extensively assessed for hydrogen injection on W7-X. The ASCOT suit of codes has been benchmarked against NUBEAM [18] and BEAM3D [19] codes. Experimental validation was performed using IR camera data and a Faraday-cup type FILD probe in W7-X [20–22], and with scintillator-based FILD measurements in the ASDEX Upgrade tokamak [23]. In all cases, the simulations showed good agreement with the experimental observations. However, to validate and build confidence in the ion modelling for future deuterium operation, the present model will first be applied to helium, acting both as the injected beam species and the target plasma. Using this model, simulations based on the parameters of specific experiments may later be compared with measurements from the recent and forthcoming W7-X campaigns. Validation will be carried out using infrared cameras to monitor hot spots on PFCs [22] and fast-ion charge-exchange spectroscopy (FIDA) to measure fast-ion velocity distributions in dedicated helium experiments. In addition, the scintillator-based fast-ion loss detector (sFILD) will provide velocity-space measurements of lost fast ions once it becomes operational in 2026, enabling comparison with synthetic signals generated using ASCOT+FILDSIM [24].

This paper is structured as follows. In section 2, the inputs of the simulation, including plasma parameters and NBI system, are presented. The behaviour of the different beam-ion species in hydrogen, deuterium and helium plasmas is analysed in detail for the standard configuration in section 3. Finally, in section 4, a comparison of beam losses and associated power loads in the STD, HM and LM configurations is presented followed by a summary and discussion of the results in section 5.

2. NBI injection and models for plasma profiles

This study was carried out using ASCOT to trace the beam ions in two stages. In the slowing-down stage, the guiding-centre orbits of the markers representing the beam ions are followed

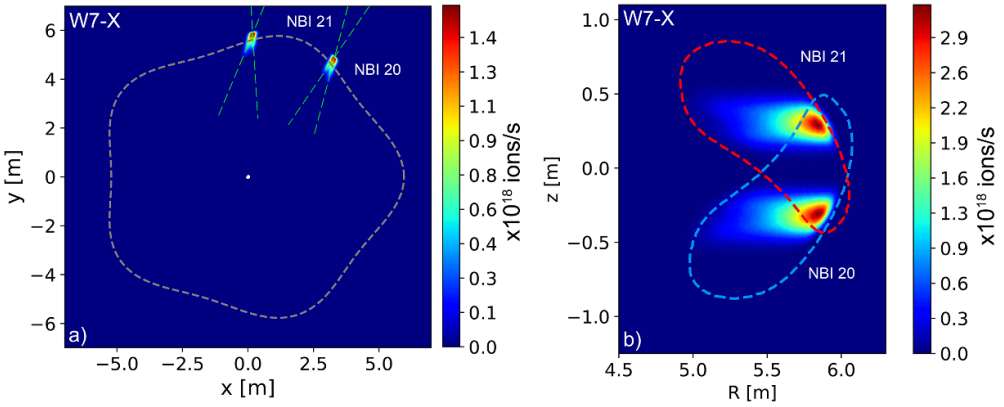

Figure 1. NBI injection from sources NBI20 and NBI21 as calculated with BBNBI for hydrogen beams in hydrogen plasma in the STD configuration. (*a*) Toroidal projection of the ionisation plume showing injection angles (dashed green) and magnetic axis (dashed grey). (*b*) Poloidal projection showing LCFS locations for NBI20 (dashed blue) and NBI21 (dashed red).

until they reach the last closed flux surface (LCFS) or thermalise. The markers at the LCFS are collected, and for each of them, multiple new markers are generated along the corresponding gyro-orbit by randomising the gyrophase. In the wall-load stage, the full orbits of the new markers are followed until they reach the walls or thermalise. The number of full-orbit markers generated from each guiding-centre marker is chosen in each case so that the size of the new ensemble is the same as the initial one. This ensures that the statistical sampling is sufficient to estimate the beam wall loads. The detailed 3D wall model, based on a CAD design of the W7-X wall structure, consists of approximately 8 M triangles.

The NBI system consists of two beam boxes (NBI20 and NBI21) with four positive ion neutral injectors (PINIs) each. Since operation with 8 beams is envisioned in future campaigns, all 8 PINIs were included in this study. Figure 1 illustrates the ionisation plume for hydrogen beams in hydrogen plasma in the STD configuration. The toroidal projection is shown in figure 1(*a*), including the magnetic axis (dashed grey) and the injection angles of the two NBI sources (dashed green). Figure 1(*b*) shows the corresponding poloidal projection, with the LCFS at the toroidal positions of NBI20 (dashed blue) and NBI21 (dashed red).

It is important to keep in mind that even though the beam lines are almost perpendicular to the plasma, the ions are born on passing or helically-trapped orbits as indicated in figure 2. This is not possible in tokamaks, where the magnetic field is axisymmetric. In stellarators, however, the intrinsically 3D magnetic field geometry enables beam injection at locations corresponding to local maxima of the magnetic field strength, allowing ions to follow passing or helically-trapped trajectories at nearly perpendicular injections. To examine these orbit types in more detail, figures 2 and 3 illustrate the main beam-ion trajectories in this study. These include passing, helically-trapped, and ripple-trapped orbits for hydrogen beams in hydrogen plasma. The observed topologies in the W7-X quasi-isodynamic configuration are consistent with those previously reported for quasi-isodynamic [3], quasi-axisymmetric, and quasi-helical equilibria [25].

Figures 2(*a*) and (*d*) show the poloidal projections of a passing orbit with initial pitch $\xi = 0.42$ and a helically-trapped orbit with initial pitch $\xi = -0.24$, respectively. In this representation, θ denotes the geometrical poloidal angle of the trajectory, as opposed to the Boozer poloidal angle. The corresponding toroidal projections are shown in figures 2(*b*) and (*e*). In both cases, ions can traverse several field periods, even for helically-trapped trajectories that exhibit turning points.

A third topology, shown in figure 3, corresponds to a ripple-trapped orbit. This case is particularly relevant to the present analysis, as ions trapped in ripple wells can drift to the walls. The orbit shown depicts an ion that initially follows as a helically-trapped trajectory ($\xi = -0.24$) and undergoes a collisionless transition to a ripple-trapped state, reaching a final pitch of $\xi = 0.04$.

In order to characterise the beam-ion confinement for current and future injection species, hydrogen, helium and deuterium were simulated separately. Also, the species of the target plasma was varied to assess its effect on the losses. For brevity, the particle species will be indicated using its symbol when referring to the beam injection (H, D and He) and the full spelling for the target plasma (hydrogen, deuterium and helium).

Each beam species has distinct injection energies. For H and D beams, the nominal full-energy components (E) are 55 keV and 60 keV, respectively. Additional half (E/2) and one-third (E/3) energy components arise from the acceleration of molecular ions and their dissociative neutralisation in the gas neutraliser. The He beam only has atomic ions, therefore, only has the nominal-energy injection at 40 keV. It is also important to notice that the beam ions of different species populate the nominal-, half- and one-third energy fractions differently. The injection energy fractions are presented in figure 4 for the three beam species. Aside from the difference in injection energies, the injected power also changes for each case. The neutralised power for the H, D and He beams are 2.5 MW, 1.8 MW, 0.75 MW per PINI, respectively.

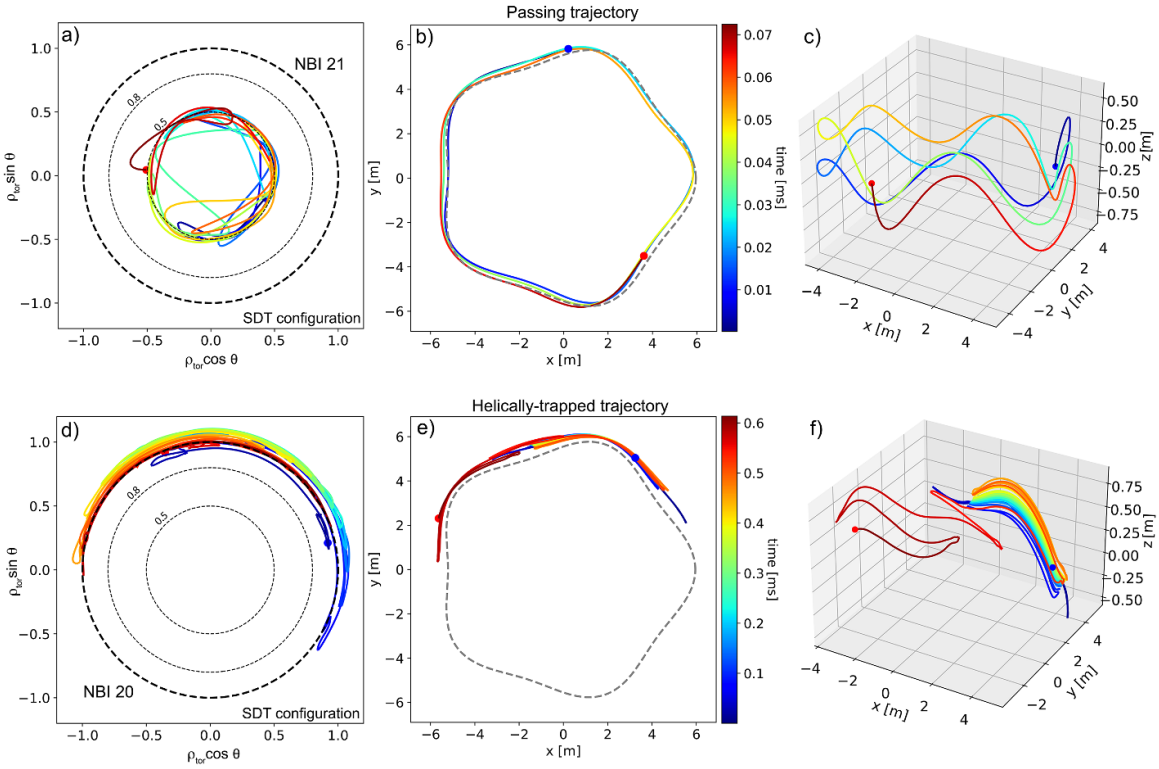

Figure 2. Passing and helically-trapped beam-ion orbits shown as poloidal (*a*), (*d*) and toroidal (*b*), (*e*) projections. In the poloidal representations, θ denotes the geometrical poloidal angle of the orbit. Dashed black lines in panels (*a*) and (*d*) indicate contours of constant toroidal flux, with thicker dashed lines marking the LCFS. The magnetic axis is indicated by a grey dashed line in panels (*b*) and (*e*). Panels (*c*) and (*f*) present the 3D representations of the orbits, with the colour bar indicating the time along each trajectory. The dots mark the initial (blue) and final (red) points of each orbit.

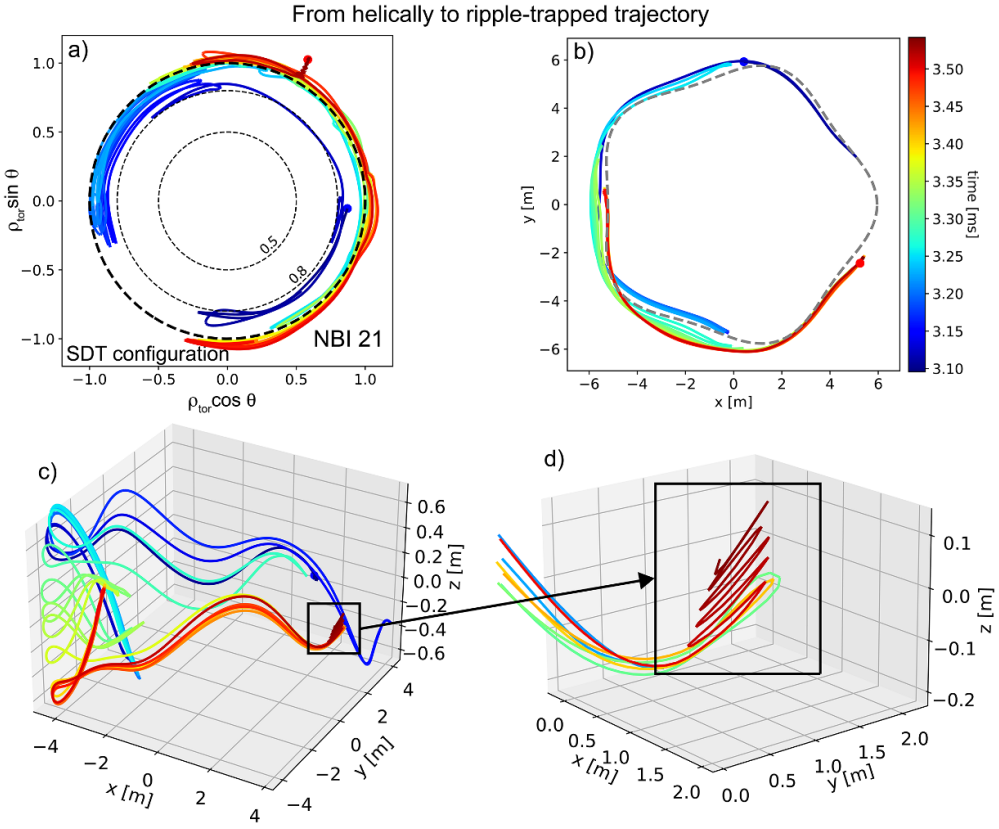

Figure 3. Transition from a helically-trapped to a ripple-trapped orbit. The poloidal and toroidal projections are shown in panels (*a*) and (*b*), respectively. The meaning of the different lines and colors are the same as in figure 2. The 3D orbit is shown in (*c*), with a zoom of the final segment in (*d*); the colour bar indicates time along the trajectory.

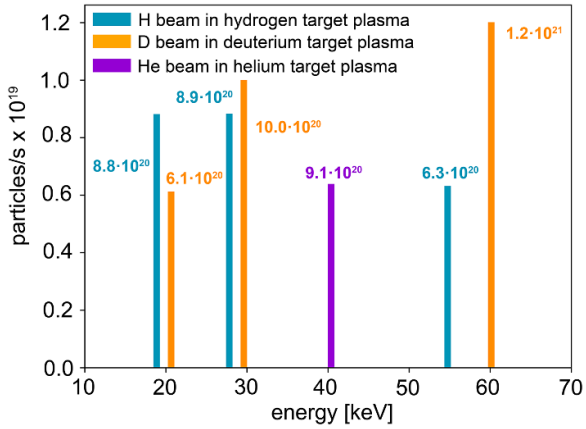

Figure 4. Relative abundance of the nominal-, half- and one-third energy fractions for the H, D and He beam-ion deposition. Values above the bars indicate the particle injection in particles/s corresponding to each energy component. Notice that for the H beam, the half and one-third energy fractions are more populated than the nominal-energy component. The He injection only exhibits the nominal-energy component as it does not form molecules.

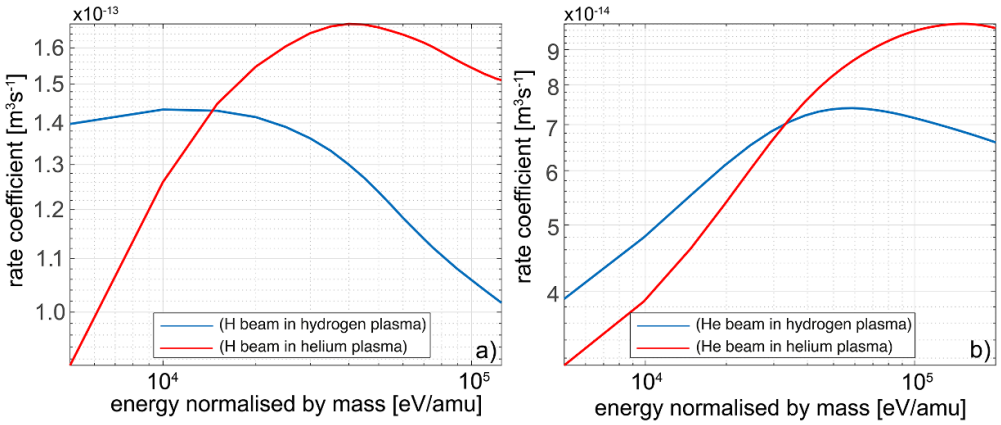

Figure 5. Non-linear contribution of the BMS coefficients as a function of mass-normalised energy for (*a*) hydrogen and (*b*) helium beams injected into hydrogen (blue) and helium (red) target plasmas.

The NBI deposition profiles were calculated using the BBNBI5 code [18], generated from the beam geometry, magnetic equilibrium and kinetic plasma profiles. The recently upgraded BBNBI5 derives the ionisation coefficients from the Atomic Data and Analysis Structure (ADAS) [26] utilising ASCOT5's atomic reactions module [27]. This new implementation is not affected by the Suzuki model limitation to hydrogenic species [28], thus enabling the generation of birth distributions for helium beams and target plasmas. To illustrate the behaviour of the beam-stopping coefficients for the species and plasma combinations considered in this study, figure 5 shows the non-linear contribution of the effective beam stopping (BMS) coefficients obtained from the ADAS database. Two important trends can be observed in this figure: the lower rate coefficients of the He beam compared to the H and D beams; and the change in relative ionisation efficiency when switching from a hydrogenic to a helium plasma, which depends on the *energy*/*amu* range of each beam injection (e.g. 10 keV/amu for He beams).

For this analysis, ad-hoc profiles that capture the essential features of the NBI operation in W7-X were used. The electron density and temperature profiles for hydrogen and deuterium plasmas are shown in figure 6 as a function of the normalised radial coordinate $\rho_{\mathrm{tor}} = \sqrt{s}$, where s is the normalised toroidal flux. These profiles were used for all magnetic configurations. In the helium plasma case, the electron density n_{e} was taken to be the same as in the hydrogen plasma, but the ion density n_{He} was halved to ensure quasineutrality, and a 5% hydrogen impurity was introduced.

The magnetic configurations analysed in this work were the so-called standard, high-mirror and low-mirror configurations [29]. The rationale behind these choices is that they present three extreme cases, which allows us to cover a wide range in terms of fast-ion confinement. The *standard* is the reference configuration, and the high- and low-mirror configurations have the best and worst fast-ion confinement according to previous studies [14, 15]. The magnetic equilibria were calculated with VMEC [30] for each configuration, and the radial electric

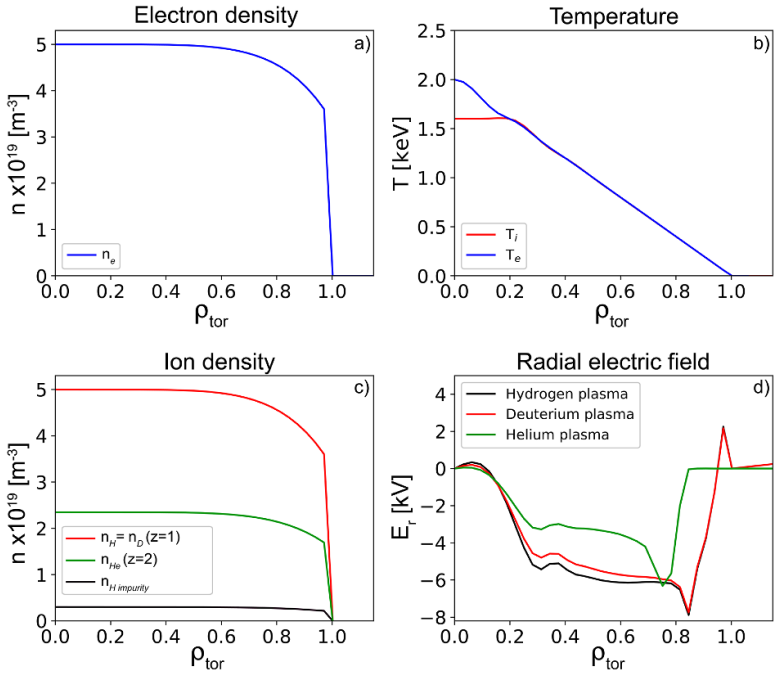

Figure 6. The radial kinetic plasma profiles for the different plasma species included in the ASCOT simulations. (*a*) The electron density. (*b*) The electron and ion temperature. (*c*) The ion density in hydrogen and deuterium plasmas (red), assumed identical to n_e; and the ion density for helium plasmas (green) with a 5% hydrogen impurity (black). (*d*) The Neotransp-calculated radial electric fields corresponding to each plasma species.

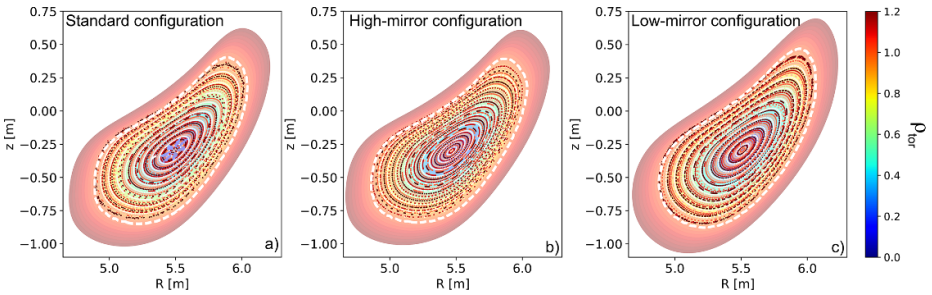

Figure 7. Poincaré plots of magnetic field lines for the STD, HM, and LM configurations, superimposed on a colour map of normalised toroidal flux ρ_{tor} at the NBI20 toroidal location. The LCFS is shown as a white dashed line.

field and bootstrap current were obtained with the Neotransp code, which integrates the mono-energetic transport coefficients from the DKES code [31] over the Maxwellian distribution, following the approach used in the NTSS code [32]. Given plasma species temperatures and densities, the code determines the radial electric field from the ambipolarity constraint. Throughout the simulations, the radial electric field profiles are kept time-independent.

To illustrate the differences between the three magnetic configurations analysed, figure 7 shows Poincaré plots of magnetic field lines from the VMEC equilibria for the STD, HM, and LM configurations. The plots are overlaid on a colour map showing contours of constant normalised toroidal flux, ρ_{tor}. The value $\rho_{\mathrm{tor}} = 1$ corresponds to the LCFS (dashed white line). It should be noted that the present simulations neglect scrape-off layer and charge-exchange effects, which may affect detailed wall-load distributions.

3. Effect of the injection and plasma species on the beam-ion confinement

This chapter examines the behaviour of beam ions in the standard magnetic configuration of W7-X, with a focus on how the interplay between beam and plasma species affects confinement and wall interactions. In particular, the analysis investigates the deposition characteristics of the injected beams, the evolution of their energy and pitch distributions, and the resulting power loads on the PFCs. It was found that several trends emerge across different combinations of beam and plasma species.

3.1. Beam deposition and ionisation profiles

The NBI deposition profiles for the standard configuration are shown in figure 8 for H, D, and He beams in hydrogen, deuterium, and helium plasmas. The number of beam ions

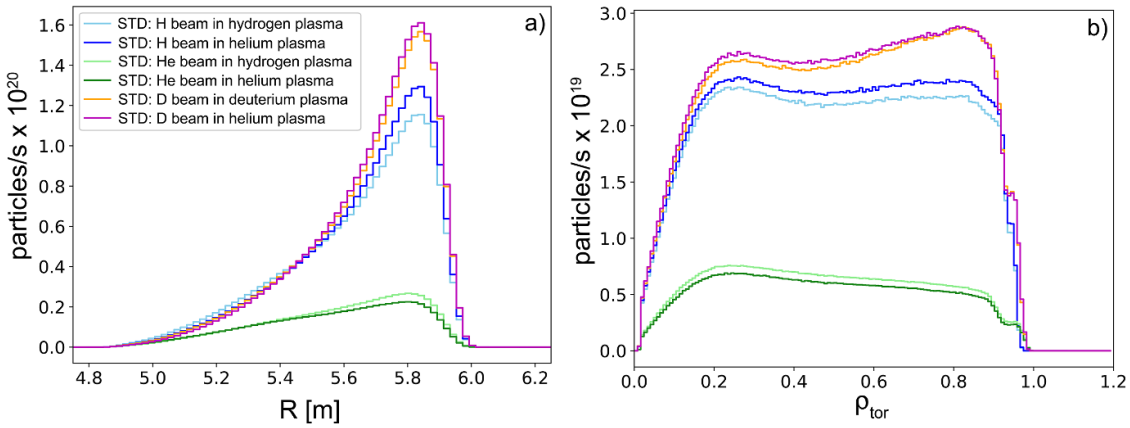

Figure 8. NBI deposition profiles for the different plasma and beam-injection species in the standard magnetic configuration as a function of (*a*) the initial major radius, R, and (*b*) initial radial coordinate ρ_{tor}. Please note that this figure does not display density but the particle rate within a given radius so it drops at the centre due to the small plasma volume.

is shown instead of their density to provide a more accurate representation of the spatial distribution across the major radius. Density plots tend to peak near the core due to smaller flux-surface volumes, which can obscure the edge-peaked nature of the NBI birth profile. The differences in the number of deposited ions arise from variations in injection energy and beam power, which determine the ionisation efficiency depending on the species combination of beam end target plasma.

The deposition profiles as a function of ρ_{tor}, presented in figure 8(*b*), indicate that ion deposition for all beams is mostly flat across the plasma. However, by comparing the hydrogenic beams injected into hydrogen plasmas, the heavier D beam displays stronger deposition at the plasma edge, whereas the H beam is able to penetrate further into the plasma. These effects can be explained in terms of the attenuation cross section of the beam, which has a strong dependency on the ion energy per mass (E/mass), shown in figure 5. For H beams, the dominant components have 20 and 30 keV (figure 4) which, at this energy range, leads to a more efficient ionisation for helium plasma than hydrogen plasma. This effect is clear in figure 5. For D beams, its nominal component at 60 keV is dominant but due to its double mass, the E/mass is at 30 keV/amu, resulting in a higher ionisation. However, the half-energy component is also significant with its E/mass of 15 keV/amu and, for that case, the ionisation coefficient is lower for helium plasma. Thus, the overall behaviour does not differ significantly.

For He beams, the lower rate coefficients presented in figure 5, lead to a deposition profile that reaches even deeper into the plasma. This can be observed in figure 8(*b*), where the profile is flatter and slightly higher at the core region. The He beam is mono-energetic at 40 keV, but has an E/mass of 10 keV, where the BMS coefficient is higher for hydrogen plasmas. This is visible in the ionisation profiles, where He deposition on hydrogen plasma is slightly higher. That the total source rate of the He beams is 10% of the hydrogenic beams is not only because the ionisation efficiency, but also because the injection power is lower. A fully ionised He^{+2} was assumed in this analysis.

The effect of the different ionisation rates is also reflected in the shinethrough fraction. When comparing hydrogenic and helium target plasmas, shinethrough in hydrogen plasmas is higher by a factor of 1.5 for H beams and 1.4 for D beams. In contrast, He beams exhibit higher shinethrough in helium plasmas, increasing by a factor of 1.3. A summary of the shinethrough behaviour is later presented in table 1.

After deposition, the beam-ion confinement was studied using a 10 million marker ensemble. Each case is identified using a label in the format (X, Y), where X represents the ion-beam species and is given as an abbreviation, while Y represents the target plasma species and is written explicitly. All cases were simulated using the two-stage scheme, first calculating the slowing-down distribution (section 3.2) and then following the markers reaching the separatrix up to the walls (section 3.3).

3.2. *Slowing-down behaviour and ion transport*

For the calculation of the slowing-down distributions, the contribution of ions is computed over time until they either thermalise or cross the LCFS. However, it should be noted that reaching the LCFS does not necessarily imply loss, as confined orbits with guiding centres moving through $\rho_{\mathrm{tor}} > 1$ regions may exist near the outer edge of the plasma. In figure 9, the slowing-down distributions are shown as a function of the energy and pitch, defined as the ratio of parallel to total velocity ($\xi = v_{\parallel}/v$). This plot consists of three pairs of figures, with each pair corresponding to one of the injected species: H, D and He. In each pair, the left plot shows the distribution for a hydrogenic target plasma, while in the right plot the beams have been injected into a helium plasma. The symmetric double-lobed pattern at positive and negative pitch values arises from half of the beams injecting in opposite directions.

A common feature across all beam species, when injected into helium plasma, is the broadening of the pitch distribution, particularly at lower energies. This broadening is caused by the increased pitch scattering resulting from stronger collisional

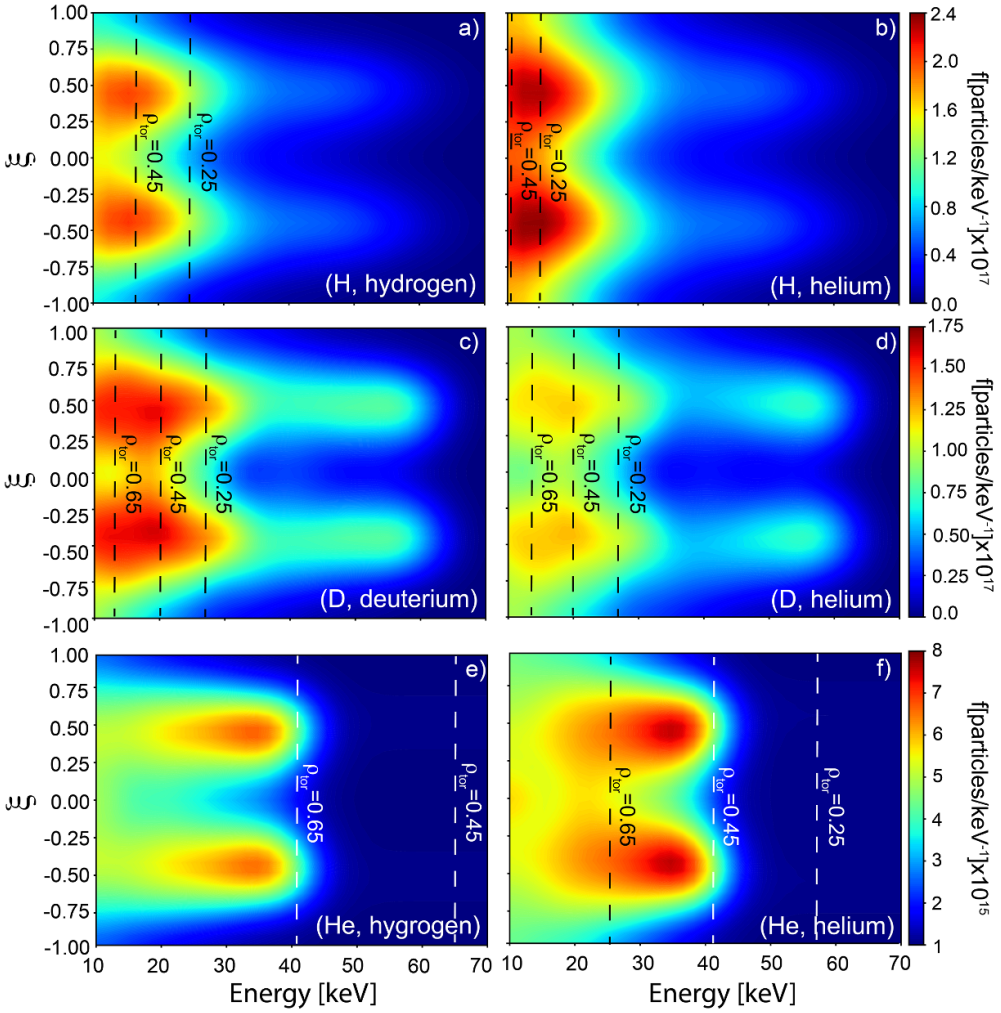

Figure 9. Slowing-down distribution of beam ions as a function of the particle energy and pitch for all analysed combinations of beams and plasma species in the standard configuration. Please note that each beam has different injection power, so relative abundances between beam cases should not be considered. E_{crit} is indicated by vertical dashed lines at the ρ_{tor} values of interest.

effects, as the interaction is twice as strong compared to hydrogenic plasmas. As expected, the effect is more pronounced at lower injection energies, which are closer to the critical energy (E_{crit}), as shown in figure 9 for relevant values of ρ_{tor}. While that aspect is shared across all cases, the following analysis focuses on case-specific behaviours. To complement the information in figure 9, table 1 summarises the key parameters for evaluating the various sources of energy loss. This includes the number of injected neutrals accounting for duct scraping losses (Injected); the shinethrough fraction (ST (%)); the total number and fraction of ionised particles lost to the walls (Ion loss and Ion loss (%), respectively); and the corresponding power loss, defined as the fraction of injected power lost through both shinethrough and ion losses (Power loss (%)). Shinethrough is defined as the ratio of the power carried by non-ionised neutrals to the injected power. These parameters are discussed further in the next section. Taking this into account, each injection is analysed separately, beginning with the H beam.

For the H beam in helium plasma (H, helium), the distribution exhibits two spots at 15 keV that are more intense than in the (H, hydrogen) case. The occurrence of these spots in both cases is due to the H beam injecting primarily half- and one-third-energy particles, so the low-energy region is well populated by both contributions. The increased intensity observed in the (H, helium) case, however, arises from higher ionisation in helium plasma, resulting in a larger number of ions. The nominal-energy ions are efficiently slowed down in both plasmas, as expected, since E_{crit} is sufficiently low for most of the plasma cross section.

In the D-beam case, the increased escaping ions relative to the H-beam case must also be considered for a meaningful comparison. In helium plasmas, deposition does not increase as significantly as it does for the H beam and, therefore, does not substantially increase the initial ion population. Instead, the higher number of escaping ions reaching the LCFS reduce the overall distribution intensity (table 1). These ions are able to reach the LCFS primarily due to the larger orbit size of deuterium ions. This effect is most pronounced for the nominal-energy component which, for D beams, is also the most populated and contributes the most to the total number of marginally-confined ions. Where ‘marginally confined’

refers to orbits that are not necessarily lost but reach the LCFS, so they stop contributing to the slowing-down distribution. The distribution also exhibits a low-pitch gap for energies below the E_{crit}, where pitch scattering dominates. In this region, the loss cone becomes visible due to ions that are scattered into trapped orbits, where confinement is less effective, ultimately contributing to increased marginally-confined population.

It is worth noting that, for a straightforward comparison between H and D beams, nominal-energy ions constitute approximately 50% of the marginally-confined population in the (H, helium) case, increasing to 60% in the (D, helium) configuration. A helium target plasma leads to a relative increase in nominal-energy ions, which in turn depletes the intermediate-energy population between nominal and half energies, resulting in a visible gap at 35–45 keV. Additionally, although all three injection energies are present in both cases, the nominal-energy component is more pronounced in the D beam compared to the H beam, reflecting the higher relative population of nominal-energy ions in deuterium injection.

For He beams, the two spots are visible only at the monoenergetic injection. In this case, the E_{crit} plays an important role as it exceeds the injection energy across the outer half of the plasma cross section and this threshold even higher for hydrogen plasmas. More quantitatively, in hydrogen plasma, only ions born outside $\rho_{\mathrm{tor}} = 0.65$ are slowed down predominantly by electrons; those born inside this radius thermalise primarily with bulk ions, which is a less efficient slowing-down mechanism. In helium plasma, E_{crit} lies further in, so that ions born beyond $\rho_{\mathrm{tor}} = 0.45$ are efficiently slowed down by electrons. This effect combined with the shape of the ionisation profile for He beams (figure 8(*b*)), which is not centrally peaked, accounts for the more pronounced slowing-down tails for helium plasma. Another factor to consider is that the ionisation profile populates the inner half of the plasma (figure 8(*b*)), where the injection energy is below E_{crit} (figures 9(*e*) and (*f*)), so that pitch scattering is already visible at the nominal 40 keV energy. Accordingly, analysing the slowing-down distributions requires taking into account not only the fraction of ions reaching the LCFS ($\rho_{\mathrm{tor}} = 1$), but also their characteristic time scales, including thermalisation and escape times. As the distribution is computed and accumulated over time, ions with longer escape times contribute over a longer period, increasing the visibility and weight of their contribution. The critical energy in helium plasmas is lower than in hydrogen plasmas. As a result, in helium plasma, the injected ions exceed this value already from $\rho_{\mathrm{tor}} = 0.45$ outward, so in most of the plasma they experience primarily electron collisions and slow down more efficiently. Consequently, the escape time in helium plasmas is about twice that in hydrogen plasmas, and these non-thermal ions have a higher contribution to the slowing-down distribution.

To further understand the impact of these mechanisms on confinement, figure 10 shows the deposition profiles with the subset of ions that reach the LCFS. This comparison indicates that the population of different energy components within the beam significantly affects the total marginally-confined ions. In this figure, dashed lines represent the ionisation profiles for each energy component, while solid lines correspond only to the ions that reach the LCFS during the slowing-down phase of the simulations.

For H injection, the highest deposition occurs in the lower energy fractions ($E/2$, $E/3$), while the nominal-energy component, which contributes most significantly to beam losses, accounts for only 25% of the total deposition. In helium plasma, the ionisation is slightly higher and the curve of ions reaching the LCFS is even bigger. Also, this curve extends to ions that may have been born on the low-field side. For D injection, it is clear that nominal- and half-energy components are most populated, constituting 78% of the injected beam. Therefore, D-beam ions are, on average, 30% more energetic than those in the H-beam case, which contributes to the higher marginally-confined ions. The behaviour is similar to the H beam, however, the increase in the ions reaching the LCFS in helium plasma is even more significant. He beams present some qualitative differences with respect to H and D. While the ionisation for both H and D beams decreases nearly exponentially with decreasing major radius (figures 10(*a*)–(*d*)), for He beams the attenuation is closer to linear (figures 10(*e*) and (*f*)). Additionally, helium plasmas affect the He beams in two ways: a flatter ionisation profile across the major radius and a slight increase in the fraction of ions reaching the LCFS at the low-field side (figure 10(*f*)).

By comparing the left and right panels of figure 10, it can be observed that helium plasmas broaden the radial reach of ion transport for all beam species. Although helium plasma has halved ion density to preserve quasineutrality, the double charge increases the intensity of the Coulomb collisions. In all cases with helium plasma, the solid curves show a higher number of ions reaching the LCFS even from the inner plasma, indicating that in helium plasmas the transport is not limited to the edge but also affects ions born deeper inside the plasma. This effect is more intense for the nominal-energy components, as is expected since transport is correlated with radial excursion of the ions.

3.3. Beam-ion losses and wall loads

In the wall-hit stage, markers that have reached the LCFS in the first stage are initialised from their last recorded location at the LCFS and are followed along their gyro orbits until they reach the wall or thermalise. The overall results are summarised in table 1 considering each contribution to the energy loss. As illustrated in figure 8, injection into helium plasmas leads to a decrease in shinethrough for H and D beams and an increase for He beams. For D beams, the beam-ion losses are increased almost by a factor of 3 compared to the H-beam case. There are two main factors contributing to this behaviour. The double mass of deuterium ions as well as their higher energy increases radial excursion by 50%. Also, D beams deposit more ions at the higher energy components (figure 4), which on average leads to wider orbits and longer mean free paths, both increasing the total losses. The slightly reduced shinethrough

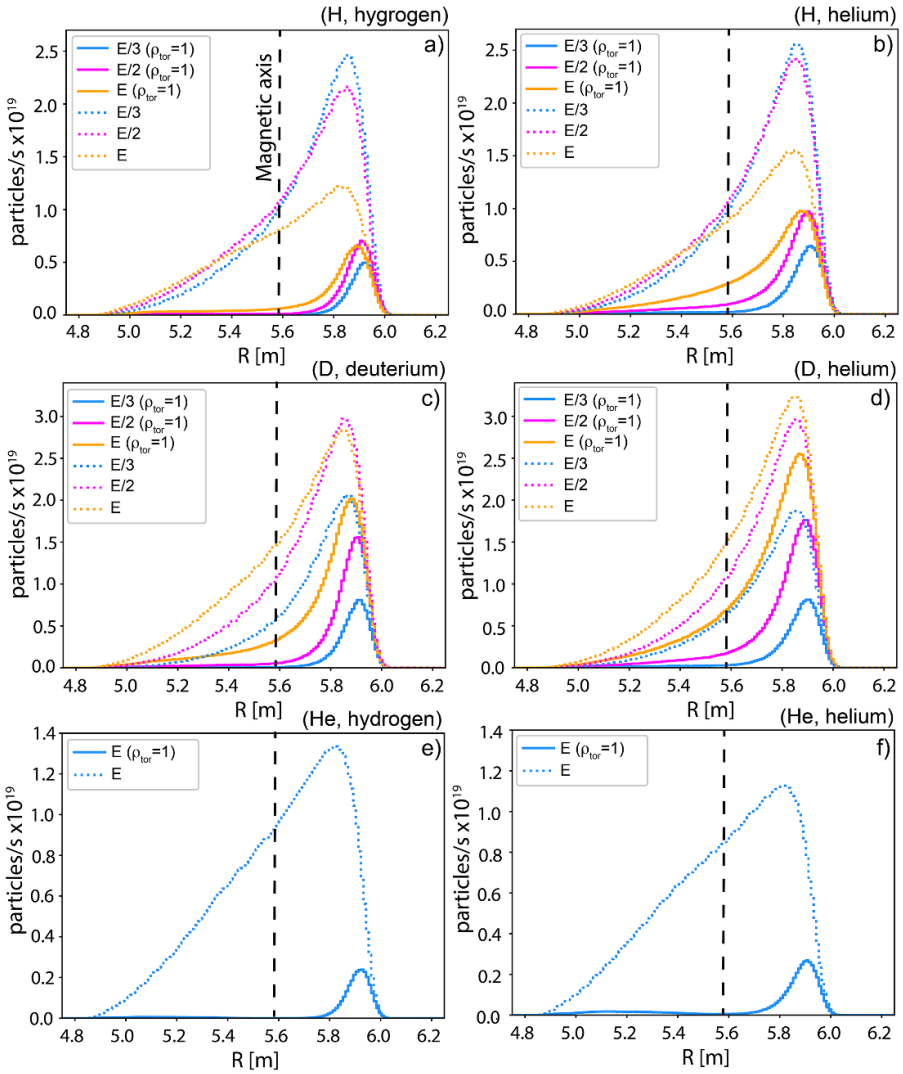

Figure 10. Deposition profiles of each energy fraction (E, $E/2$, $E/3$) of the H, D and He beams are indicated with dashed lines for hydrogen, deuterium and helium plasmas. The solid line stands for only those ions that reached the LCFS before thermalising.

Table 1. Summary of injected neutrals, including port losses (Injected), shinethrough fraction (ST), total number of lost ions (Ion loss), lost-ion fraction (Ion loss (%)), and total power-loss fraction (including both ion loss and shinethrough) in the STD configuration for all the analysed combinations of injection and target plasma species.

Case	Injected (neutrals/s)	ST (%)	Ion loss (ion/s)	Ion loss (%)	Power loss (%)
(H, hydrogen)		16.2	2.8e+20	11.8	23.6
(H, helium)	2.7e+21	10.5	5.7e+20	22.9	25.9
(D, deuterium)		8.4	8.5e+20	30.1	29.9
(D, helium)	3.0e+21	6.0	1.3e+21	43.9	38.9
(He, hydrogen)		24.5	2.8e+19	4.0	26.2
(He, helium)	9.4e+20	31.6	4.3e+19	6.7	33.9

for the D beam has both a positive and a negative effect on the power loss. On the one hand, it lowers the total power loss but on the other hand, it increases the ion population in the plasma, leading to larger ion-losses. This is more visible for D beams, where the nominal-energy dominates. He beams exhibit the lowest ionisation efficiency, with shinethrough levels that are 1.5 times higher than those of H beams in hydrogen plasmas, and 3 times higher in helium plasmas. The ion-loss fraction is lower as the slowing-down times are also shorter.

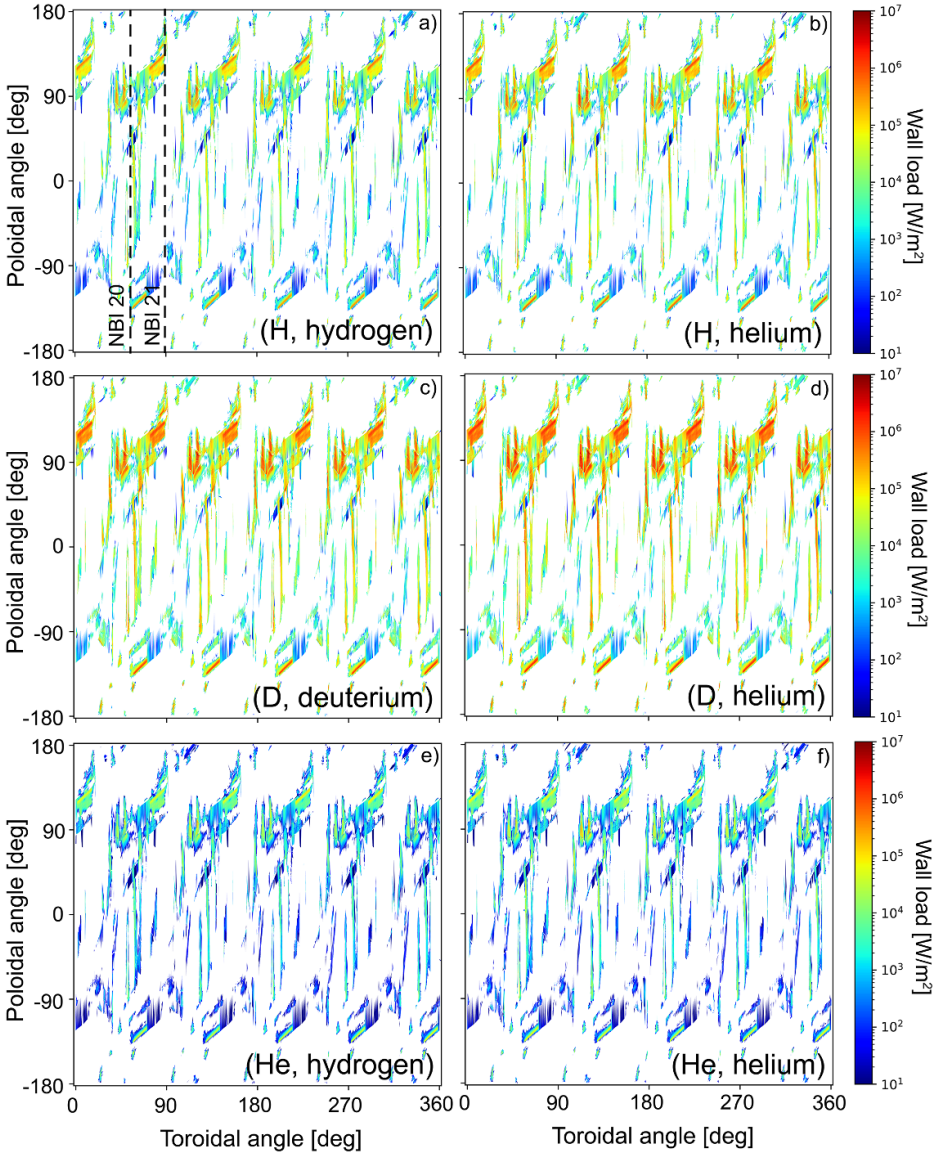

Figure 11. A 2D representation of the wall power loads is presented for the injections of (H, hydrogen), (H, helium), (D, deuterium), (D, helium), (He, hydrogen), and (He, helium) in the STD configuration. The power loads to the wall, expressed in terms of power per unit area, are shown on a logarithmic scale, incorporating contributions exclusively from beam losses while excluding shinethrough. The vertical black dashed line denotes the toroidal location of the NBI boxes.

In all beam cases, the effect of changing the target plasma species to helium enhances the ions losses. The increase corresponds to a factor of 2 for H beams, 1.5 for D beams, and 1.7 for He beams. This result can be understood by studying the differences in the pitch scattering and slowing down in helium plasmas. As was shown in figure 9, the pitch scattering is visibly stronger for helium plasmas for all beam species. Another contributing factor to the loss differences between H and D beams in helium plasma can be inferred from the birth profiles in figure 8(*b*). These profiles indicate that, in helium plasmas, H-beam ionisation leads to a greater fraction of particles born near the edge compared to hydrogen plasmas, whereas this difference is much smaller in the D-beam case. This contributes to the larger relative increase in beam losses observed for H beams.

The total power loss is a combination of the shinetrough and the beam-ion losses. However, shinetrough has a stronger effect on the power loss as these lost particles failing to ionise leave the plasma at full energy. This results in the He beams having more power loss than H beams with only one third of the beam-ion losses.

Having analysed the impact of beam and plasma species on total ion losses, it is of great practical interest to assess how these losses translate into power loads on the vessel wall. To this end, figure 11 presents the wall load distributions for all cases summarised in table 1. The 2D histograms represent toroidal—poloidal projections of the wall loads, allowing for direct comparison of the deposition patterns across cases. To ensure the accuracy of the power-load results, a convergence test of the peak loads was performed as a function of the number of sampled markers using the bootstrap-

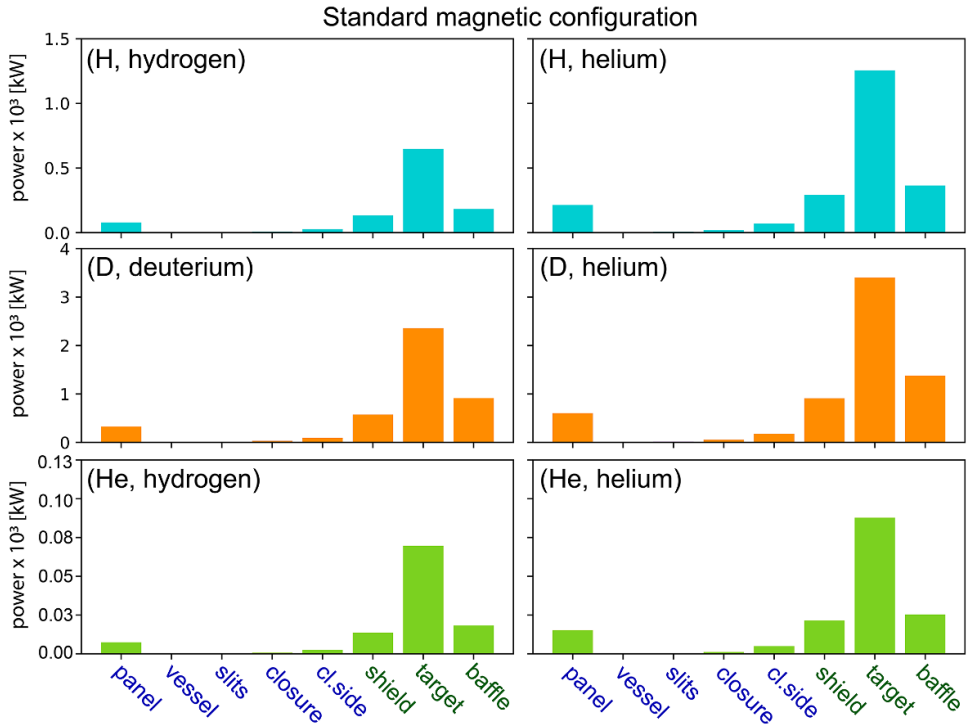

Figure 12. Power loads to the different wall components in kW for a beam and target plasma species in the standard configuration. Blue labels indicate steel components while green labels correspond to carbon components.

Table 2. Power loads to the wall components in kW for a beam and target plasma species in the standard configuration. Blue labels indicate steel components while green labels correspond to carbon components.

Case	Panel	Vessel	Slits	Closure	Cl. side	Shield	Target	Baffle
(H, hydrogen)	78.6	1.0	3.6	7.8	26.5	133.1	648.5	183.3
(H, helium)	213.3	2.8	7.6	18.2	70.8	291.8	$1.3{\cdot}10^{3}$	364.4
(D, deuterium)	326.7	2.5	9.4	31.2	91.1	574.5	$2.4{\cdot}10^{2}$	914.1
(D, helium)	602.7	4.9	13.9	52.6	178.1	910.6	$3.4{\cdot}10^{3}$	$1.4{\cdot}10^{3}$
(He, hydrogen)	7.4	$9.1{\cdot}10^{-2}$	0.3	0.7	2.5	13.6	69.7	18.2
(He, helium)	15.2	0.2	0.4	1.1	5.0	21.5	87.8	25.3

ping method. According to the test, stable results are obtained already with an ensemble of $5 \cdot 10^6$ markers, so the size of the ensemble used in this study, 10^7, exceeds that with good margin.

In all cases, the shape of the power loads is similar, indicating that the wall patterns are determined only by the magnetic configuration, the wall shape and the beam-injection geometry. However, the intensity of the loads is affected by both the beam and plasma species. The wall patterns are independent of the sector, as shown in figure 11(*a*). This implies that the main contribution to the wall loads comes from ions able to travel around the torus before escaping, which is consistent with the orbits shown in figures 2 and 3.

To better characterise the spatial distribution of power deposition, figure 12 summarises the load profiles on various PCF components, distinguishing between the vulnerable steel (panel, vacuum vessel, pumping slits, closure, closure side) and more robust carbon elements (heat shield, divertor baffle, divertor target). The corresponding quantitative values of power deposition are reported in table 2. A 3D view of the vacuum vessel, indicating the various wall components for clarity, is shown in figure A1 in appendix. For all beam species, the majority of the power is deposited on the carbon components, as expected. However, the steel panels also receive a noticeable fraction of the load, particularly for the D-beam injection, where the steel load can reach up to 13% of the total deposited power. Additionally, power loads are highest when beams are injected into helium plasmas.

In terms of the power-load magnitude, both H and D beams exhibit peak values on the order of 1–3 MW m^{-2}, with the D beam reaching levels approximately 2 to 3 times higher than the H beam. In contrast, He beams result in the lowest power loads, approximately one order of magnitude lower. This substantial reduction in He-beam power loads arises from a combination of factors: lower relative ion losses and reduced injected power compared to the hydrogenic beams. Additionally, all beams show a clear increase in power loads when injected into helium plasmas, ranging from a factor of 1.2 for He beams to a factor of 2 for H beams.

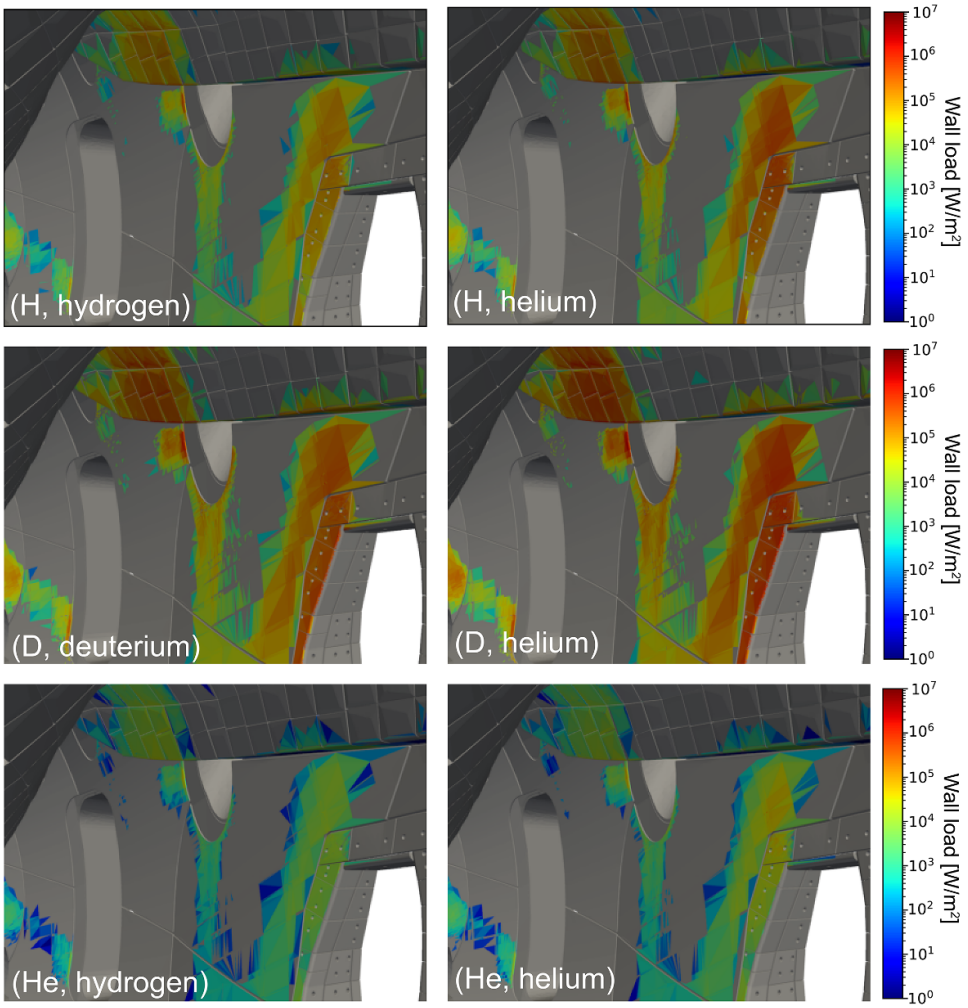

Figure 13. 3D view of the beam-ion power loads, given in MW m^{-2}, at the region surrounding one F-port for the different cases of beam and plasma species in the STD configuration.

In addition to the total power loads, it is essential to evaluate the power per unit area on the more delicate components. Figure 13 presents a perspective view of the power loads on the PFCs in module 2 for all cases. The view is centred on the upper F-port, where the leading edges of the surrounding stainless-steel panels exhibit heat loads increasing from 1 MW m^{-2} in the (H, hydrogen) case to 3 MW m^{-2} in the (D, helium) case. The maximum value of 3 MW m^{-2} remains within the established safety limits for steel components, though only for pulse durations shorter than 0.1 s based on estimations from previous studies [14, 33].

3.4. Orbit topologies and velocity-space of lost beam ions

The orbit topologies responsible for wall loads can be analysed in figure 14, which shows the velocity-space distributions of beam ions lost to the walls as a function of energy and pitch (ξ) at the point of wall impact. For the H and D beams, the nominal-, half- and one-third energy fractions are visible, along with their respective slowing-down tails. In the H-beam case, the power loads predominantly originate from the half- and one-third energy components, whereas for the D beam, the nominal- and half-energy fractions contribute most significantly. These results are consistent with the different population of the injection energies for each beam. For the He beam, the distribution shows a single dominant spot, with its sole injection energy and accompanied by a pronounced slowing-down tail. This behaviour can be attributed to the lower critical energy in helium plasmas, which enhances the efficiency of the slowing-down process and results in more extended energy tails in the lost-ion distribution.

The (D, helium) case provides particularly useful insight, as the distribution of lost ions complements the features observed in the slowing-down distributions. Specifically, the lower intensity of the nominal-energy component and the absence of ions between the half- and nominal-energy levels in figure 9(*d*) are explained by the corresponding loss distribution shown in figure 14(*d*), which occupies the same region in the velocity space. In comparison, the (D, deuterium) case (figure 14(*c*)), exhibits less pronounced loss tails, consistent with the more distinct presence of those components in the slowing-down distribution (figure 9(*c*)).

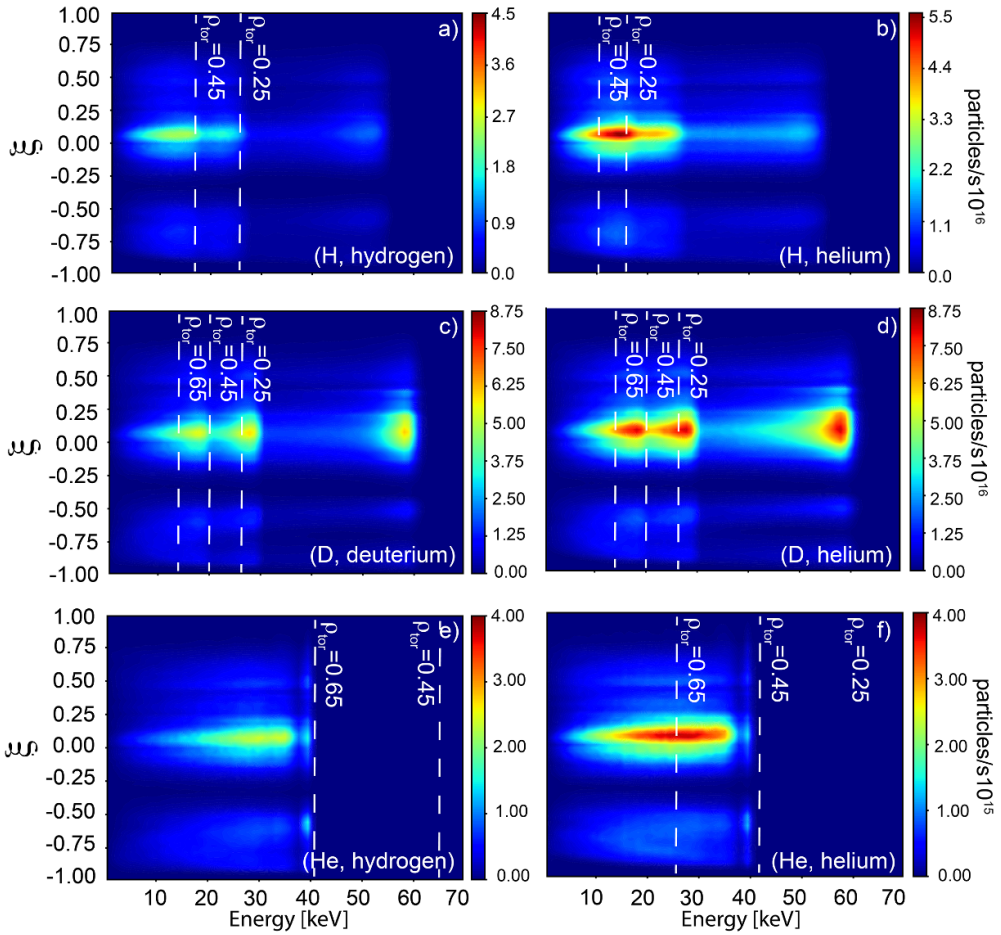

Figure 14. Pitch-energy distribution of beam ions at the point of wall impact for all combinations of beam and plasma species in the STD configuration. E_{crit} is indicated by vertical dashed lines at the ρ_{tor} values of interest.

In all cases, the majority of beam ions contributing to wall loads have pitch $\xi \approx 0.1$ at the point of impact. This is an expected result as the ripple grows close to the walls and the ions become trapped in the ripple wells. The large aspect ratio of W7-X implies small banana widths, so it is only ripple-trapped ions that reach the walls. The initial orbit topology is inferred from figure 11, which shows toroidally uniform power loads with no significant enhancement near the NBI boxes. This suggests that lost ions originate on passing and helically-trapped orbits, become trapped in ripple wells, and are subsequently lost in different modules. Unlike in tokamaks, this mechanism occurs in stellarators even without collisions, allowing ions at injection energy to reach wall regions throughout the device.

A weaker loss region is also observed between $\xi \approx 0.5$ and $\xi \approx 0.8$, corresponding to helically-trapped ions, which follow trapped orbits but can drift into other modules after a few poloidal transits. Additionally, a minor contribution from passing orbits is visible near $\xi \approx -0.9$ for all injection species.

The losses are also asymmetric in pitch, reflecting the combined influence of the injection angle and the wall geometry. In a quasi-isodynamic device such as W7-X, reversing the parallel velocity does not change the orbit topology, so co- and counter-going ions follow similar trajectories. Minor differences may still occur because reversed orbits trace the sequence of field-strength extrema in the opposite order, leading to small drifts. However, these effects remain secondary compared with the much stronger influence of the injection angle and the associated wall-interaction patterns for each direction.

4. Comparison of the power loads due to beam-ion losses in the STD, LM and HM magnetic configurations

To complete this study, the HM and LM configurations were analysed in terms of beam losses, including both shinethrough and beam-ion losses. For these simulations, the kinetic plasma profiles were the same as for the standard configuration, whereas the radial electric fields were recalculated with Neotransp for each case.

Table 3 summarises the results for both configurations, considering the same cases as in the STD configuration. When compared to the STD configuration, the HM configuration yields broadly similar results in terms of neutral beam losses and power deposition. For both H and D-beam injections, shinethrough levels remain nearly unchanged across all target

Table 3. Summary of injected neutrals, including port losses (Injected), shinethrough fraction (ST), total number of lost ions (Ion loss), lost-ion fraction (Ion loss %), and total power-loss fraction (including both ion loss and shinethrough) in the HM and LM configurations for all analysed combinations of beam and target plasma species. Results for the STD configuration are included for direct comparison.

Case	Injected (neutrals/s)	ST (%)	Ion loss (ion/s)	Ion loss (%)	Power loss (%)
Standard configuration					
(H, hydrogen)		16.2	$2.8 + 10^{20}$	11.8	23.6
(H, helium)	$2.7 + 10^{21}$	10.5	$5.7 + 10^{20}$	22.9	25.9
(D, deuterium)		8.4	$8.5 + 10^{20}$	30.1	29.9
(D, helium)	$3.0 + 10^{21}$	6.0	$1.3 + 10^{21}$	43.9	38.9
(He, hydrogen)		24.5	$2.8 + 10^{19}$	4.0	26.2
(He, helium)	$9.4 + 10^{20}$	31.6	$4.3 + 10^{19}$	6.7	33.9
High-mirror configuration					
(H, hydrogen)		15.8	$2.8 + 10^{20}$	11.5	23.2
(H, helium)	$2.5 + 10^{21}$	10.1	$4.2 + 10^{20}$	16.6	21.3
(D, deuterium)		8.1	$8.3 + 10^{20}$	29.4	30.2
(D, helium)	$3.0 + 10^{21}$	5.8	$1.0 + 10^{21}$	34.7	32.6
(He, hydrogen)		24.1	$3.1 + 10^{19}$	4.1	25.7
(He, helium)	$9.3 + 10^{20}$	31.0	$3.6 + 10^{19}$	5.1	32.8
Low-mirror configuration					
(H, hydrogen)		15.2	$3.7 + 10^{20}$	15.1	24.4
(H, helium)	$2.5 + 10^{21}$	9.6	$7.1 + 10^{20}$	26.9	27.0
(D, deuterium)		7.6	$9.3 + 10^{20}$	32.6	30.2
(D, helium)	$3.0 + 10^{21}$	5.4	$1.3 + 10^{21}$	45.3	38.1
(He, hydrogen)		23.2	$3.9 + 10^{19}$	5.4	25.5
(He, helium)	$9.3 + 10^{20}$	30.2	$5.7 + 10^{19}$	8.7	33.1

plasma species. In the case of hydrogenic target plasmas, the fraction of beam-ion losses is also comparable between the two configurations. In helium plasmas, however, a reduction in beam-ion losses is observed, resulting in a lower total power loss: from 25.9% to 21.3% percent for H beams, and from 38.9% percent to 32.6% percent for D beams, relative to the STD configuration. For He injections, both shinethrough and power losses are slightly reduced in the HM case. Figure 15, which displays the power loads on the PFCs, shows that the spatial distribution of power remains largely unchanged, with most of the deposited power concentrated on the divertor and heat-shield elements in both configurations.

In the LM configuration, there is an increase in the beam-ion losses compared to the STD configuration. However, the shinethrough is reduced, leading to similar values of the total power-loss fractions for all beam and target plasma species. The power loads on the PFCs (figure 15) indicate that, although the wall-integrated power loads are comparable with the STD and HM configurations, the distribution has a relevant difference for the LM configuration. In this case, the more vulnerable steel components receive a negligible fraction of power loads, while 97% and 99% of the loads are concentrated on the shield, target and baffle structures for hydrogen and helium target plasmas, respectively.

5. Conclusions

This work analysed the effect of different beam and target-plasma species, including hydrogen, deuterium, and helium, on beam-ion losses across three magnetic configurations relevant for fast-ion confinement: the standard, high-mirror, and low-mirror configurations. Beam shinethrough, ion losses, and total power loads on PFCs were evaluated for each case.

Results from the standard configuration show that D beams produce higher ion losses than H beams, primarily due to their larger radial excursion. Losses also increase when the target plasma is changed from a hydrogenic species to helium, due to stronger pitch scattering. For H beams, the losses increase by a factor of 2 in helium plasmas, and by a factor of 1.5 for D beams. In hydrogenic plasmas, the shinethrough is higher, increasing by a factor of 1.5 for H beams and 1.4 for D beams compared with helium plasmas. However, because the total power loss reflects the combined effect of shinethrough and beam-ion losses, the reduction in shinethrough is outweighed by the increase in beam-ion losses. As a result, the total power-loss fraction increases by a factor of 1.1 for H beams and 1.3 for D beams. For He beams, both shinethrough and beam-ion losses increase in helium target plasmas, leading to a factor of 1.3 increase in the total power-loss fraction. Although the

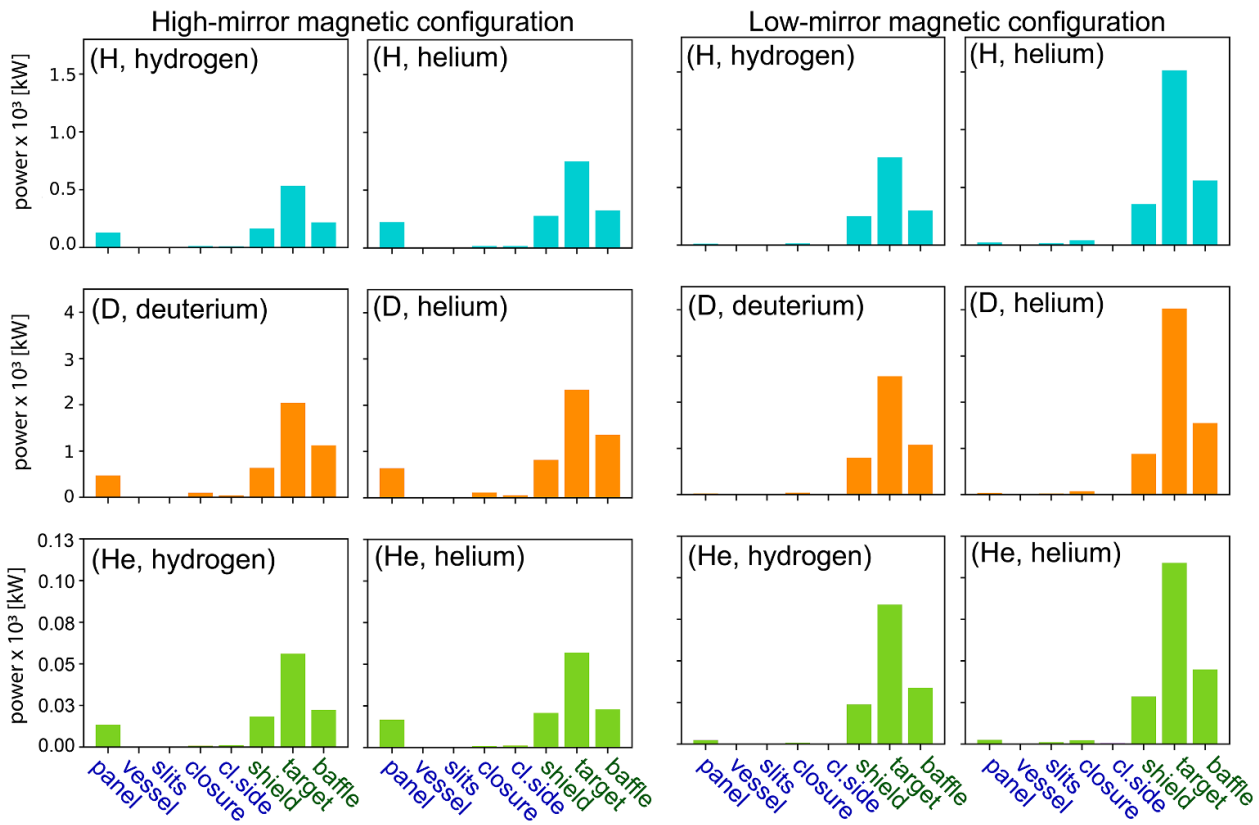

Figure 15. Power loads to the vessel components in kW for different beam and target plasma species in the low-mirror configuration. Blue labels indicate steel components while green labels correspond to carbon components.

He beam shows higher relative ion losses, its lower injection energy and power result in a comparable absolute power loss.

Calculations of power deposited per unit area were used to compare wall loads across cases, with focus on the hot spots located on the steel panels surrounding the F-ports. The results indicate that D beams can generate loads of up to 3 MW m^{-2}, whereas the loads associated with H and He beams remain at approximately 1 MW m^{-2}. The evaluation of power loads demonstrated that the wall load pattern depends solely on the magnetic configuration and wall geometry, and is independent of the beam or plasma species. Additionally, the similarity of wall loads across different toroidal modules suggests that beam-ion losses are not primarily due to first-orbit losses from the neutral beam injection. Most beam ions contributing to the power loads are helically-trapped particles whose orbits have altered from their initial topology due to ripple-well trapping or Coulomb collisions before impacting the walls.

To provide a comprehensive analysis, the low-mirror and high-mirror configurations were also included considering hydrogen, deuterium and helium as both beam and target plasmas. While the low-mirror configuration exhibits slightly higher beam-ion losses and the high-mirror configuration slightly lower losses, the comparison showed that all configurations produce similar wall-integrated power loads for all injection cases. In all the analysed magnetic configurations, most of the power due to ion losses is deposited on the carbon components as expected. An extreme case of this behaviour is the low-mirror configuration, where 97%–99% of the power loads are deposited on the carbon components, preventing the heating up of the more delicate steel components.

As noted in section 2, these simulations do not include scrape-off layer or charge-exchange effects, which may influence the final wall-load distributions [34]. While including these effects is important for improving the accuracy of hot-spot estimations, the results presented here provide a first step in characterising species-dependent transport and the mechanisms driving beam-ion losses. Building on these results, future studies will incorporate scrape-off layer and charge-exchange effects to provide a broader assessment of wall loads.

Acknowledgments

This work has been carried out within the framework of the EUROfusion Consortium, funded by the European Union via the Euratom Research and Training Programme (Grant Agreement No. 101052200 - EUROfusion). Views and opinions expressed are however those of the author(s) only and do not necessarily reflect those of the European Union or the European Commission. Neither the European Union nor the European Commission can be held responsible for them. The simulations were partly performed on the LEONARDO supercomputer (CINECA) under project reference FUA38_ASCOT_3D.

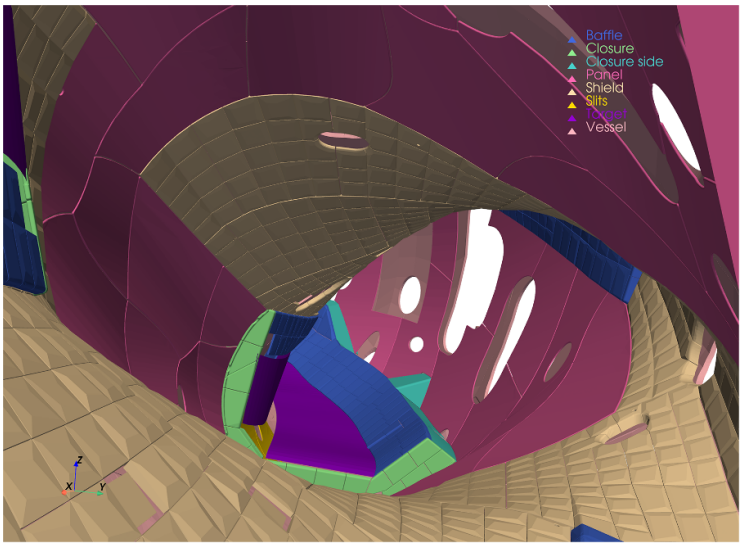

Figure A1. Internal view of the vacuum vessel showing the wall components.

Appendix. 3D view components

Figure A1 presents the detailed 3D geometry of the W7-X vessel, derived from CAD models, highlighting the various wall components. Based on their resistance to heat loads, these can be grouped into less load-resistant steel components (panel, vacuum vessel, pumping slits, closure, and closure side) and more robust carbon elements (heat shield, divertor baffle, and divertor target).

ORCID iDs

L. Sanchis 0000-0001-8211-3356
K. Särkimäki 0000-0001-9156-2559
P. Ollus 0000-0003-2558-1457
J. Kontula 0000-0002-0620-6208
S. Äkäslompolo 0000-0002-9554-5147
S. Lazerson 0000-0001-8002-0121
S. Bozhenkov 0000-0003-4289-3532
H.M. Smith 0009-0000-8071-0990

References

[1] McNeely P. *et al* 2020 Commissioning and initial operation of the W7-X neutral beam injection heating system *Fusion Eng. Des.* **161** 111997
[2] Lazerson S. *et al* 2021 First neutral beam experiments on Wendelstein 7-X *Nucl. Fusion* **61** 096008
[3] Faustin J.M. *et al* 2016 Fast particle loss channels in Wendelstein 7-X *Nucl. Fusion* **56** 092006
[4] Zonca F. *et al* 2002 Energetic particle mode stability in tokamaks with hollow q-profiles *Phys. Plasmas* **9** 4939
[5] Garcia-Munoz M. *et al* 2008 Fast-Ion losses due to high-frequency MHD perturbations in the ASDEX Upgrade Tokamak *Phys. Rev. Lett.* **100** 055005
[6] Garcia-Munoz M. *et al* 2010 Convective and diffusive energetic particle losses induced by shear Alfvén waves in the ASDEX Upgrade Tokamak *Phys. Rev. Lett.* **104** 185002
[7] Garcia-Munoz M. *et al* 2011 Fast-ion transport induced by Alfvén eigenmodes in the ASDEX Upgrade tokamak *Nucl. Fusion* **51** 103013
[8] Garcia-Munoz M. *et al* 2009 Scintillator based detector for fast-ion losses induced by magnetohydrodynamic instabilities in the ASDEX upgrade tokamak *Rev. Sci. Instrum.* **80** 053503
[9] Paz-Soldan C. *et al* 2015 Observation of a multimode plasma response and its relationship to density pumpout and edge-localized mode suppression *Phys. Rev. Lett.* **114** 105001
[10] Garcia-Munoz M. *et al* 2013 Plasma Physics and Controlled Fusion Fast-ion losses induced by ELMs and externally applied magnetic perturbations in the ASDEX Upgrade tokamak and the ASDEX Upgrade Team *Plasma Phys. Control. Fusion* **55** 124014
[11] Van Zeeland M.A. *et al* 2015 Fast ion transport during applied 3D magnetic perturbations on DIII-D *Nucl. Fusion* **55** 073028
[12] Sanchis L. *et al* 2019 Characterisation of the fast-ion edge resonant transport layer induced by 3D perturbative fields in the ASDEX Upgrade tokamak through full orbit simulations *Plasma Phys. Control. Fusion* **61** 014038
[13] Varje J. et al 2019 High-performance orbit-following code ASCOT5 for Monte Carlo simulations in fusion plasmas (arXiv:1908.02482)
[14] Akaslompolo S. *et al* 2018 Modelling of NBI ion wall loads in the W7-X stellarator *Nucl. Fusion* **58** 082010
[15] Kontula J. *et al* 2023 Predictive simulations of NBI ion power load to the ICRH antenna in Wendelstein 7-X *Plasma Phys. Control. Fusion* **65** 075008
[16] Van Zeeland M.A. *et al* 2024 Isotope impact on Alfvén eigenmodes and fast ion transport in DIII-D *Nucl. Fusion* **64** 056033
[17] Heidbrink W.W. *et al* 2025 Dependence of ion-cyclotron range of frequencies instabilities on species mix and fast-ion distribution: III. Novel sub-cyclotron modes *Nucl. Fusion* **65** 116023

[18] Asunta O. *et al* 2015 Modelling neutral beams in fusion devices: beamlet-based model for fast particle simulations *Comput. Phys. Commun.* **188** 33–46
[19] Lazerson S. *et al* 2020 Validation of the BEAMS3D neutral beam deposition model on Wendelstein 7-X *Nucl. Fusion* **60** 076020
[20] Akaslompolo S. *et al* 2019 Validating the ASCOT modelling of NBI fast ions in Wendelstein 7-X stellarator *J. Instrum.* **14** C10012
[21] Akaslompolo S 2019 Armoring of the Wendelstein 7-X divertor-observation immersion-tubes based on NBI fast-ion simulations *Fusion Eng. Des.* **146** 862–5
[22] Akaslompolo S. *et al* 2019 Validating fast-ion wall-load IR analysis-methods against W7-X NBI empty-torus experiment *J. Instrum.* **14** 07018
[23] Seppo S. *et al* 2021 ASCOT orbit-following simulations of ion cyclotron heating with synthetic fast ion loss diagnostic: a first application to ASDEX Upgrade *Nucl. Fusion* **61** 086026
[24] Galdon J. *et al* 2020 *Plasma Phys. Control. Fusion* **60** 105005
[25] Paul E.J. *et al* 2022 Energetic particle loss mechanisms in reactor- scale equilibria close to quasisymmetry *Nucl. Fusion* **62** 126054
[26] ADAS Atomic Data and Analysis Structure (available at: www.adas.ac.uk) (Accessed 29 July 2021)
[27] Ollus P. *et al* 2022 Simulating the impact of charge exchange on beam ions in MAST-U *Plasma Phys. Control. Fusion* **64** 035014
[28] Suzuki S. *et al* 1998 Attenuation of high-energy neutral hydrogen beams in high-density plasmas *Plasma Phys. Control. Fusion* **40** 2097–111
[29] Geiger J. *et al* 2015 Physics in the magnetic configuration space of W7-X *Plasma Phys. Control. Fusion* **57** 014004
[30] Hirshman S.P. and Whiston J.C. 1983 Steepest-descent moment method for three-dimensional magnetohydrodynamic equilibria *Phys. Fluids* **12** 26
[31] van Rij W.I. and Hirshman S.P. 1989 Variational bounds for transport coefficients in three-dimensional toroidal plasmas *Phys. Fluids B* **1** 563
[32] Turkin Y. *et al* 2011 Neoclassical transport simulations for stellarators *Phys. Plasmas* **18** 022505
[33] Peacock A. *et al* 2011 The procurement and testing of the stainless steel in-vessel panels of the Wendelstein 7-X Stellarator *Fusion Eng. Des.* **86** 1706–9
[34] Kiviniemi T.P. *et al* 2025 The role of SOL plasma in the confinement of NBI fast ions in W7-X *Nucl. Fusion* **67** 025034